The Astrophysical Journal, 636:1121–1134, 2006 January 10

GRAVOTURBULENT FORMATION OF PLANETESIMALS

A. Johansen, H. Klahr, and Th. Henning
Max-Planck-Institut für Astronomie, Königstuhl 17, 69117 Heidelberg, Germany
Received 2005 April 28; accepted 2005 September 14

ABSTRACT

We explore the effect of magnetorotational turbulence on the dynamics and concentrations of boulders in local box simulations of a sub-Keplerian protoplanetary disk. The solids are treated as particles, each with an independent space coordinate and velocity. We find that the turbulence has two effects on the solids. (1) Meter and decameter bodies are strongly concentrated, locally up to a factor of 100 times the average dust density, whereas decimeter bodies only experience a moderate density increase. The concentrations are located in large-scale radial gas density enhancements that arise from a combination of turbulence and shear. (2) For meter-sized boulders, the concentrations cause the average radial drift speed to be reduced by 40%. We find that the densest clumps of solids are gravitationally unstable under physically reasonable values for the gas column density and for the dust-to-gas ratio due to sedimentation. We speculate that planetesimals can form in a dust layer that is not in itself dense enough to undergo gravitational fragmentation, and that fragmentation happens in turbulent density fluctuations in this sublayer.

Subject headings: instabilities — MHD — planetary systems: formation — planetary systems: protoplanetary disks — turbulence

1. INTRODUCTION

Planets are believed to form from micrometer-sized dust grains that grow by collisional sticking in protoplanetary gas disks (Safronov 1969; see reviews by Lissauer [1993] and Beckwith et al. [2000]). Once the bodies reach a size of around 1 km, the growth to Moon-sized protoplanets and later real planets is achieved by gravitationally induced collisions (Thommes et al. 2003). Although significant progress has been made in the understanding of the initial conditions of grain growth (Henning et al. 2006), we nevertheless do not yet have a complete picture of how the solids grow 27 orders of magnitude in mass to form kilometer-sized planetesimals.

Growth by coagulation can take place when there is a relative speed between the solids. Various physical effects induce relative speeds at different grain size scales. This allows for a definition of distinct steps in the growth from micrometer dust grains to meter-sized boulders in a turbulent protoplanetary disk. Microscopic dust grains gain their relative speed due to Brownian motion. This process forms relatively compact cluster-cluster aggregates (Dominik & Tielens 1997). The speed of the Brownian motion falls rapidly with increasing grain mass, and so the timescale for building up larger compact bodies this way becomes prohibitively large compared to the lifetime of a protoplanetary disk.

When Brownian motion is no longer important, the relative speed is dominated by the differential vertical settling in the disk. The vertical component of the central star's gravity causes the gas to be stratified. Dust grains do not feel the pressure gradient of the gas and thus continue to fall toward the midplane with a velocity given by the balance between vertical gravity and the drag force. Larger grains fall faster than smaller grains due to the size-dependent coupling to the gas (actually, bodies that are so massive that they are starting to decouple from the gas will instead move on inclined orbits relative to the disk, i.e., perform damped oscillations around the midplane). As they fall, they are thus able to sweep up smaller grains in a process that is qualitatively similar to rainfall in the Earth's atmosphere. Upon arrival at the midplane, the largest solids can reach sizes of a few centimeters (Safronov 1969). These bodies have grown as compact particle-cluster aggregates with a high porosity.

Turbulent gas motions cause the sedimented solids to diffuse away from the midplane (Cuzzi et al. 1993; Dubrulle et al. 1995), where they can meet and collide with a reservoir of microscopic grains. These tiny grains still hover above the midplane because their sedimentation timescale is so long that turbulent diffusion can keep them well mixed with the gas over a large vertical extent. Turbulence also plays a role for equal-sized macroscopic bodies by inducing a relative collision speed that is much larger than the Brownian motion contribution (Völk et al. 1980; Weidenschilling 1984).

When estimating the outcome of an interaction between macroscopic bodies, the issues of collision physics must be taken into account. For relative speeds above a certain threshold, the bodies are likely to break up when they collide, rather than to stick (Chokshi et al. 1993; Blum & Wurm 2000). This is a problem for macroscopic bodies where the sticking threshold is a few meters per second. Fragmentation caused by high-speed encounters continuously replenishes the reservoir of microscopic dust grains. These can then be swept up by the boulders that are lucky enough to avoid critical encounters. However, the sweeping up of smaller dust grains by a macroscopic body has its limitations when the relative speed exceeds some 10 m s^{-1} (Wurm et al. 2001). At larger relative velocities of up to 100 m s^{-1}, which are likely to occur due to the high speed of larger bodies, the small grains will erode the boulder.

The time evolution of the size distribution of solids can be calculated by solving the coagulation equation numerically (e.g., Wetherill 1990; Weidenschilling 1997; Suttner & Yorke 2001). Recently, Dullemond & Dominik (2005) performed numerical simulations of the coagulation for realistic disk environments. Starting with micrometer-sized grains only, they find that a narrow peak of 0.1–10 m sized boulders can form in 10^4–10^5 yr, when fragmentation is ignored. On the other hand, in a more realistic situation high-speed impacts lead to fragmentation. Here Dullemond & Dominik (2005) find that once the size distribution reaches the meter regime, still around 80% of the mass is maintained in microscopic bodies, which are the fragments of larger

bodies that have been destroyed in collisions. This picture is given some credit by the fact that microscopic dust grains are observed in protoplanetary disks of millions of years of age, whereas the timescale for depleting grains of those sizes is only around 1000 yr in the absence of fragmentation.

Besides the problem of getting macroscopic bodies to stick, meter-sized boulders quickly drift radially inward toward the central star due to their aerodynamic friction with the gas in a typical sub-Keplerian disk (Weidenschilling 1977). The drift timescale can be as short as 100 yr. To avoid evaporation in the inner disk or in the central star, the bodies must grow by least an order of magnitude in size (3 orders of magnitude in mass) in a time shorter than this!

A way to overcome the growth obstacles was suggested independently by Safronov (1969) and by Goldreich & Ward (1973). The general idea is that boulders sediment toward the midplane and form a particle sublayer that undergoes a gravitational instability, forming the planetesimals in a spontaneous event (*gelation*) rather than by continuous growth (*coagulation*). The weakest point in this model is that it requires a laminar disk in order to work. Even a tiny amount of turbulence in the disk will prevent the boulders from an efficient sedimentation toward the midplane, and the instability will never occur (Weidenschilling & Cuzzi 1993). Thus disk turbulence always had to be avoided in order to allow for self-gravity-assisted planetesimal formation. However, even in a completely laminar disk, the settled dust induces a vertical shear in the gas rotation profile (Weidenschilling 1980; Nakagawa et al. 1986). This can be unstable to a Kelvin-Helmholtz instability. The subsequent Kelvin-Helmholtz turbulence puffs up the dust layer so that the densities needed for a gravitational instability are usually not achieved, unless a dust-to-gas ratio many times higher than the solar composition is adopted (Youdin & Shu 2002).

Nevertheless, solids can reach sizes of around 1 m without the help of self-gravity. In this size regime the gradual decoupling from the gas motion enables the bodies to move independently from the gas. This can cause them to be trapped in turbulent features of the gas flow. An important theoretical discovery is that meter-sized boulders are concentrated in gaseous anticyclonic vortices (Barge & Sommeria 1995; Chavanis 2000; Johansen et al. 2004). Inside such vortices the dust density can locally be enhanced to values sufficient either for enhanced coagulation or even for gravitational fragmentation. Also, the radial drift of particles trapped in the vortices is significantly reduced (de la Fuente Marcos & Barge 2001). Theoretical attention has furthermore been given to the trapping of dust grains in high-pressure regions. Since dust grains do not feel pressure forces, any pressure-supported gas structure must cause dust grains to move in the direction of the pressure gradient (Klahr & Lin 2001; Haghighipour & Boss 2003; Klahr & Lin 2005). Recently, Rice et al. (2004) demonstrated that this can lead to large concentrations (a density increase of up to a factor of 50) of meter-sized boulders in the high-density spiral arms of self-gravitating disks. The same mechanism can drain millimeter-sized dust grains from the underdense regions around a protoplanet that is not massive enough to open a gap in the gaseous component of the disk (Paardekooper & Mellema 2004).

Giant long-lived vortices may form in protoplanetary disks due to a baroclinic instability (Klahr & Bodenheimer 2003), but the conditions for the baroclinic instability in protoplanetary disks are still not clear (Klahr 2004). Magnetorotational turbulence (MRI), on the other hand, is expected to occur in all disks where the ionization fraction is sufficiently high (Gammie 1996; Fromang et al. 2002; Semenov et al. 2004). A search for dust concentrations in magnetorotational turbulence was done by Hodgson & Brandenburg (1998), who found no apparent concentrations. On the other hand, recently Johansen & Klahr (2005, hereafter JK05) found evidence for centimeter-sized dust grains being trapped in short-lived turbulent eddies present in magnetorotational turbulence. That work was, however, limited by the fluid description of dust grains— i.e., the friction time must be much shorter than the orbital period—and could not handle grains larger than a few centimeters.

In this paper, we expand the work done in JK05 by putting meter-sized dust particles, represented by real particles rather than by a fluid, into magnetorotational turbulence. We show that magnetorotational turbulence (Balbus & Hawley 1991) is not actually an obstacle to the self-gravity-aided formation of planetesimals, but rather can be a vital agent to produce locally gravitational unstable regions in the solid component of the disk when the average density in solids would not allow for fragmentation. This process is very similar to the gravoturbulent fragmentation of molecular clouds into protostellar cores (Klessen et al. 2000; Padoan & Nordlund 2004).

2. DYNAMICAL EQUATIONS

For the purpose of treating meter-sized dust boulders we have adapted the Pencil Code[1] to include the treatment of solid bodies as particles with a freely evolving (x, y, z)-coordinate on top of the grid. This is necessary because the mean free path of the boulders, with respect to collisions with the gas molecules, is comparable to the scale height of the disk. Thus the dust component can no longer be treated as a fluid, but must be treated as particles, each with a freely evolving spatial coordinate $\boldsymbol{x}_i$ and velocity vector $\boldsymbol{v}_i$. In other words, it is no longer possible to define a unique velocity field at a given point in space for the particles, because they keep a memory of their previous motion. Friction only erases this memory for small grains.

2.1. *Drag Force*

The particles are coupled to the gas motion by a drag force that is proportional to the velocity difference between the particles and the gas,

$$\boldsymbol{f}_{\rm drag} = -\frac{1}{\tau_f}\,(\boldsymbol{v}_i - \boldsymbol{u}). \tag{1}$$

Here $\boldsymbol{u}$ is the gas velocity at the location of particle i, and τ_f is the friction time. The friction time depends on the solid radius $a_\bullet$ and the solid density $\rho_\bullet$ as

$$\tau_f = \frac{a_\bullet^2 \rho_\bullet}{\min(a_\bullet c_s,\, 9/2\nu)\rho}, \tag{2}$$

where ν is the molecular viscosity of the gas, c_s is the sound speed, and ρ is the gas density. This expression is valid when the particle speed is much lower than the sound speed (Weidenschilling 1977). Using the kinetic theory expression for viscosity $\nu = c_s\lambda/2$, where λ is the mean free path of the gas molecules, the friction time can be divided into two regimes: the Epstein regime is valid when $a_\bullet < 9/4\lambda$. Here the mean free path of the gas molecules is longer than the size of the dust grain, so the gas cannot form any flow structure around the object. The friction time is proportional to the solid radius in this regime. In the Stokes

[1] The code is available at http://www.nordita.dk/software/pencil-code; see also Brandenburg (2003).

regime, where $a_\bullet > 9/4\lambda$, a flow field forms around the object. Now the friction time is proportional to the solid radius squared, so the object decouples faster from the gas with increasing size. For an isothermal and unstratified disk, one can treat the friction time τ_f as a constant. The distinction between the Epstein and the Stokes regime is then only important for translating the friction time into a solid radius (see end of this section).

To determine the gas velocity in equation (1) at the positions of the particles, we use a three-dimensional first-order interpolation scheme, using the eight grid corner points surrounding a given particle. For multiprocessor runs, the particles can move freely between the spatial intervals assigned to each processor using Message Passing Interface (MPI) communication.

2.2. *Disk Model*

We consider a protoplanetary disk in the shearing sheet approximation with a global pressure gradient $\partial \ln P/\partial \ln r = \alpha$ (or $P \propto r^\alpha$) through the box. In the shearing sheet approximation this gradient produces a constant additional force that points radially outward (because the pressure falls outward). Making the variable transformation $\ln \rho \rightarrow \ln \rho + (1/r_0)\alpha x$, the standard isothermal shearing sheet equation of motion (e.g., Goldreich & Tremaine 1978) gets an extra term,

$$\frac{\partial \boldsymbol{u}}{\partial t} + (\boldsymbol{u}\cdot\nabla)\boldsymbol{u} = -2\boldsymbol{\Omega}_0 \times \boldsymbol{u} + 3\Omega_0^2 \boldsymbol{x} - c_s^2 \nabla \ln \rho - c_s^2 \frac{1}{r_0}\alpha \hat{\boldsymbol{x}}. \quad (3)$$

The terms on the right-hand side of equation (3) are the Coriolis force, the centrifugal force plus the radial gravity expanded to first order, and the two terms representing the local and global pressure gradient. The coordinate vector (x, y, z) is measured from the comoving radial position $\boldsymbol{r}_0$ from the central source of gravity, with x pointing radially outward and y along the Keplerian flow. At $r = r_0$ the Keplerian frequency is Ω_0. The shearing sheet approximation is valid when all distances are much shorter than r_0. The balance between pressure gradient, centrifugal force, and gravity is given for a sub-Keplerian rotation of the disk,

$$u_y^{(0)} = -\frac{3}{2}\Omega_0 x + \frac{c_s^2}{2\Omega_0}\frac{1}{r_0}\alpha, \quad (4)$$

where the first term on the right-hand side is the purely Keplerian rotation profile, while the second (constant) term is the adjustment due to the global pressure gradient. We now measure all velocities relative to the sub-Keplerian flow using the variable transformation $\boldsymbol{u} \rightarrow \boldsymbol{u} + \boldsymbol{u}_0$, where $\boldsymbol{u}_0 = u_y^{(0)}\hat{\boldsymbol{y}}$. This changes equation (3) into

$$\frac{\partial \boldsymbol{u}}{\partial t} + (\boldsymbol{u}\cdot\nabla)\boldsymbol{u} + u_y^{(0)}\frac{\partial \boldsymbol{u}}{\partial y} = \boldsymbol{f}(\boldsymbol{u}) - c_s^2 \nabla \ln \rho. \quad (5)$$

Here the last term on the left-hand side represents the advection due to the rotation of the disk relative to the center of the box (which moves on a purely Keplerian orbit). The function $\boldsymbol{f}$ is defined as

$$\boldsymbol{f}(\boldsymbol{u}) = \begin{pmatrix} 2\Omega_0 u_y \\ -\frac{1}{2}\Omega_0 u_x \\ 0 \end{pmatrix}. \quad (6)$$

When making the same variable transformation in the equation of motion of the dust particles, there is, however, no global pressure gradient term to balance the extra Coriolis force imposed by the sub-Keplerian part of the motion, so the result is

$$\frac{\partial \boldsymbol{v}_i}{\partial t} = \boldsymbol{f}(\boldsymbol{v}_i) - \frac{1}{\tau_f}(\boldsymbol{v}_i - \boldsymbol{u}) + c_s^2 \frac{1}{r_0}\alpha \hat{\boldsymbol{x}}. \quad (7)$$

The modified Coriolis force $\boldsymbol{f}$ appears again because of the presence of $x_i(t)$ in $\boldsymbol{u}_0$. The last term on the right-hand side reflects the head wind that the dust feels when it moves through the slightly sub-Keplerian gas. The reason why the term appears in the radial component of the equation of motion is because all velocities are measured relative to the rotational velocity of the gas. A dust particle moving at zero velocity with respect to the gas thus experiences an acceleration in the radial direction.

The explicit presence of r_0 in equation (7) is nonstandard in the shearing sheet. It may seem that the term vanishes for $r_0 \rightarrow \infty$. But this is actually not the case, since the natural timescale of the disk, Ω_0^{-1}, also depends on r_0, so that at large radii there is an immense amount of time at hand to let the tiny global pressure gradient force work. One can quantify this statement by dividing and multiplying by the scale height H in the last term of equation (7) to obtain the result

$$\frac{\partial v_x^{(i)}}{\partial t} = \ldots + c_s \Omega_0 \frac{H}{r_0}\alpha. \quad (8)$$

Here $H/r_0 \equiv \xi$ is the ratio of the scale height to the orbital radius, a quantity that is below unity for thin disks. Depending on the temperature profile of a disk, the typical value of ξ is between 0.001 and 0.1. We define the pressure gradient parameter β as $\beta \equiv \alpha\xi$.

For the simulations, we adopt the following dynamical equations for gas velocity $\boldsymbol{u}$, magnetic vector potential $\boldsymbol{A}$, gas density ρ, particle velocities $\boldsymbol{v}_i$, and particle coordinates $\boldsymbol{x}_i$:

$$\frac{\partial \boldsymbol{u}}{\partial t} + (\boldsymbol{u}\cdot\nabla)\boldsymbol{u} + u_y^{(0)}\frac{\partial \boldsymbol{u}}{\partial y} = \boldsymbol{f}(\boldsymbol{u}) - c_s^2 \nabla \ln \rho + \frac{1}{\rho}\boldsymbol{J}\times\boldsymbol{B} + \boldsymbol{f}_\nu(\boldsymbol{u}, \rho), \quad (9)$$

$$\frac{\partial \boldsymbol{A}}{\partial t} + u_y^{(0)}\frac{\partial \boldsymbol{A}}{\partial y} = \boldsymbol{u}\times\boldsymbol{B} + \frac{3}{2}\Omega_0 A_y \hat{\boldsymbol{x}} + \boldsymbol{f}_\eta(\boldsymbol{A}), \quad (10)$$

$$\frac{\partial \rho}{\partial t} + \boldsymbol{u}\cdot\nabla\rho + u_y^{(0)}\frac{\partial \rho}{\partial y} = -\rho\nabla\cdot\boldsymbol{u} + f_{\rm D}(\rho), \quad (11)$$

$$\frac{\partial \boldsymbol{v}_i}{\partial t} = \boldsymbol{f}(\boldsymbol{v}_i) - \frac{1}{\tau_f}(\boldsymbol{v}_i - \boldsymbol{u}) + c_s \Omega_0 \beta \hat{\boldsymbol{x}}, \quad (12)$$

$$\frac{\partial \boldsymbol{x}_i}{\partial t} = \boldsymbol{v}_i + u_y^{(0)}\hat{\boldsymbol{y}}. \quad (13)$$

The functions $\boldsymbol{f}_\nu$, $\boldsymbol{f}_\eta$, and $f_{\rm D}$ are hyperdiffusivity terms present to stabilize the finite difference numerical scheme of the Pencil Code. This is explained in more detail in JK05. We ignore the effect of the global pressure gradient on the dynamics of the gas, since for $\xi \ll 1$ the increase in density due to the global gradient is much smaller than the average density in the box. Thus we set simply $u_y^{(0)} = -3/2\Omega_0 x$. We also ignore the contribution from the global density on the Lorentz force term in equation (9) and the advection of global density in equation (11). Furthermore, we do not include vertical gravity in the simulations. This means that we solve exactly the same equations for the gas as in JK05, i.e., without radial pressure stratification. The radial drift of solids then originates exclusively from the dynamical equations of the particles.

TABLE 1
Simulation Parameters

Run (1)	N (2)	$L_x \times L_y \times L_z$ (3)	$n_x \times n_y \times n_z$ (4)	n_0 (5)	$\Omega_0 \tau_f$ (6)	β (7)	Δt (8)
A	2×10^6	$1.32 \times 1.32 \times 1.32$	$64 \times 64 \times 64$	7.6	1.0	−0.04	100
B	2×10^6	$1.32 \times 1.32 \times 1.32$	$64 \times 64 \times 64$	7.6	0.1	−0.04	100
C	2×10^6	$1.32 \times 1.32 \times 1.32$	$64 \times 64 \times 64$	7.6	10.0	−0.04	100
D	2×10^6	$1.32 \times 1.32 \times 1.32$	$64 \times 64 \times 64$	7.6	1.0	0.00	100
E	2×10^6	$1.32 \times 5.28 \times 1.32$	$64 \times 256 \times 64$	1.9	1.0	−0.04	24
F	2×10^6	$1.32 \times 10.56 \times 1.32$	$64 \times 512 \times 64$	1.0	1.0	−0.04	16

Notes.—Col. (1): Name of run. Col. (2): Number of particles. Col. (3): Size of the box measured in scale heights. Col. (4): Grid dimension. Col. (5): Number of particles per grid cell. Col. (6): Friction time. Col. (7): Global pressure gradient parameter. Col. (8): Number of orbits that the simulation has run.

We solve the dynamical equations (9)–(13) for various values of the friction time and of the box size. The typical resolution is 64^3 for a box size of $1.32H$ on all sides. A similar setup was used in JK05 to calculate the turbulent diffusion coefficient of dust grains in magnetorotational turbulence. In the present work we expand the model by letting 2,000,000 particles represent the dust grains. Thus the dust component is typically represented by approximately eight particles per grid cell. We set the strength of the radial pressure gradient by the parameter $\beta = -0.04$. This would represent, e.g., a disk with a global pressure gradient given by $\alpha = -1$ and a scale height–to–radius ratio of $\xi = 0.04$, which is typical for a solar nebula model (Weidenschilling & Cuzzi 1993). We consider friction times of $\Omega_0 \tau_f = 0.1, 1,$ and 10. The translation from friction time into grain size depends on whether the friction force is in the Epstein or in the Stokes regime, but the two drag laws yield quite similar grain sizes in the transition regime. Thus at the radial location of Jupiter in a typical protoplanetary disk, the friction time corresponds to grains of approximately 0.1, 1, and 10 m in size.

The simulation parameters are given in Table 1. We let the boulders have random initial positions from the beginning and let them start with zero velocity.

3. PARTICLE CONCENTRATIONS

In Figure 1 we plot the number of particles in the densest grid cell as a function of time for run A (meter-sized boulders; see Table 1). The average number of particles per grid cell is 7.6. Evidently there are more than 100 particles in the densest grid cell at most of the times, and at some times the number is even above 600. This is more than 80 times the average dust number density. In Figure 2 we plot the maximum particle density for runs with $\Omega_0 \tau_f = 0.1$ (run B, *gray curve*) and $\Omega_0 \tau_f = 10$ (run C, *black curve*). The decimeter-sized boulders are obviously not as strongly concentrated as the meter-sized boulders, whereas the decameter-sized boulders have concentrations that are similar in magnitude to run A. The measured values of the maximum particle density for all the runs can be found in Table 2.

To examine whether some structures in the gas density are the source of the high particle densities, we plot in Figure 3 the column densities of gas Σ and of dust particles Σ_d at a time of 50.9 orbits for run A. The gas column density varies only by a few percent over the box, since the turbulence is highly subsonic, but a region of moderate overdensity is seen around the middle of the box. The dust column density is very high in about the same region as the gas overdensity, around a factor of 5 higher than the average dust column density in the box, so dust particles have moved from the regions that are now underdense into the overdensity structure near the center of the box.

We explore the radial density structure of the gas and the dust in the box in more detail in Figure 4. Here the azimuthally averaged gas and dust column densities are shown as a function of radial position x and time t measured in orbits. Apparently, large-scale

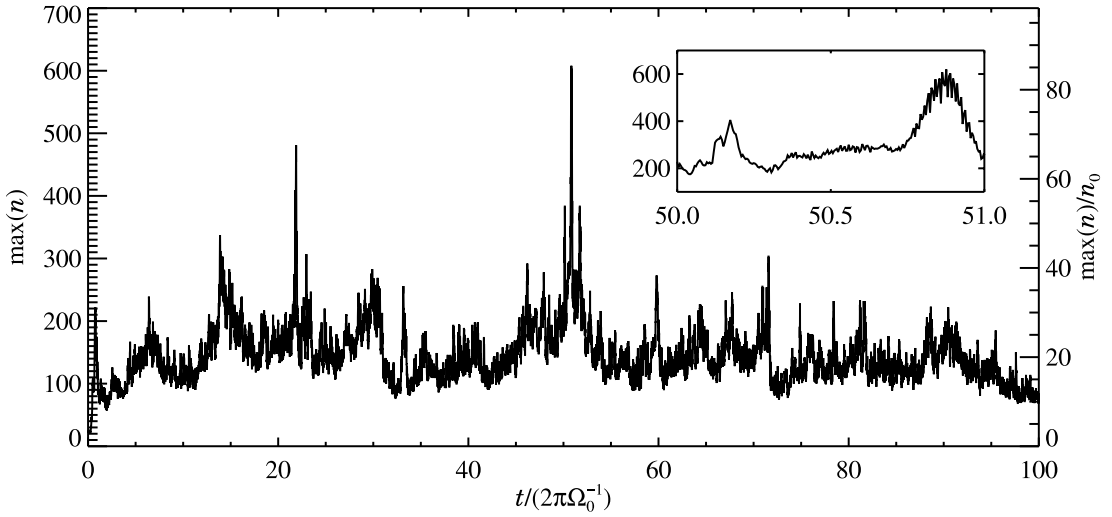

Fig. 1.—Number of particles in the densest grid cell as a function of time for run A (meter-sized boulders). The maximum density is generally around 20 times the average, but peaks at above 80 times the average particle density. The inset shows a magnification of the time between 50 and 51 orbits.

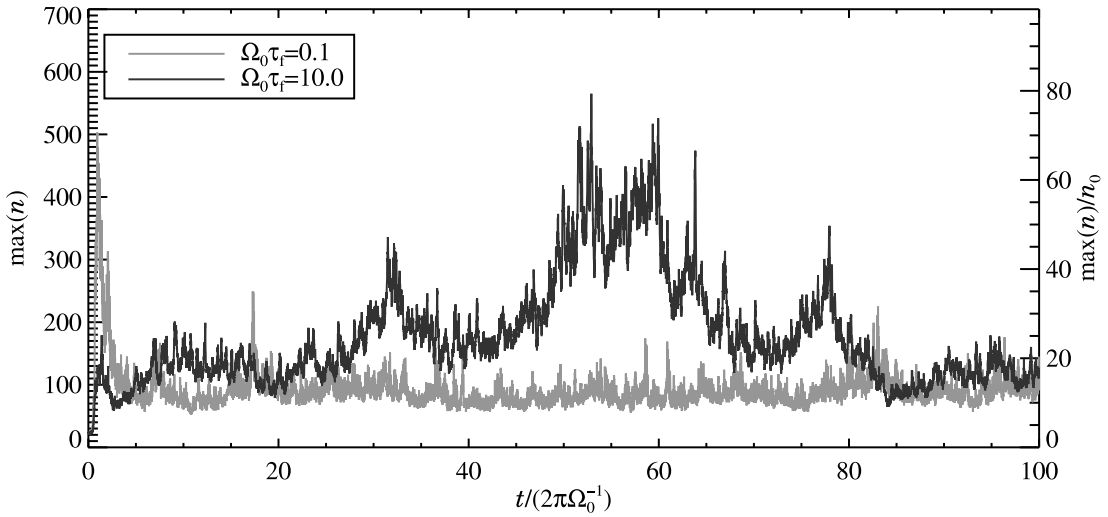

FIG. 2.—Number of particles in the densest grid cell as a function of time, here for runs B (decimeter-sized boulders) and C (decameter-sized boulders). The first shows only very moderate overdensities, whereas the latter is similar in magnitude to run A (meter-sized boulders), but with broader peaks.

gas density fluctuations live for a few orbits at a constant radial position before decaying and reappearing at another radial position. The fluctuation strength is less than 1% of the average density. The dust density shows strong peaks at the locations of the gas density maxima. The explanation for this correlation is as follows. Locations of maximal gas density are also local pressure maxima. Such pressure maxima can trap dust grains (Klahr & Lin 2001; Haghighipour & Boss 2003), as they are locations of Keplerian gas motion. The inner edge of a pressure maximum must move faster than the Keplerian speed because the pressure gradient mimics an additional radial gravity. At the outer edge of a radial pressure enhancement the outward-directed pressure gradient mimics a decreased gravity, and the gas must move slower than the Keplerian speed. Dust grains do not feel the pressure gradient and are thus forced to move into the pressure bump. In our simulations the radial gas overdensities have a typical lifetime at a given radial position on the order of a few orbits. When the gas overdensity eventually disappears, the particle overdensity is only slowly getting dissolved, and the particles drift and concentrate toward the location of the next gas overdensity. The gas density structure in the azimuthal and vertical directions does not show a similar density increase, and as expected there is also no significant concentration of particles with respect to these two directions. The density fluctuations thus have the form of two-dimensional sheets.

In Figure 5 we plot the maximum density experienced by a 200 particle subset of the 2,000,000 particles during the 100 orbits. The distribution function $\xi(n)$ is defined as the fraction of particles that have been the center of a number density of at least n over the size of a grid cell. The curves clearly show how large the concentrations are. For decimeter-sized boulders, 95% of them have experienced a 5-fold increase in dust density, whereas only around 2% have been part of a 10-fold increase. For meter-sized particles, 70% have been part of a 10-fold increase in dust density. Particles of decameter-size had more than 10% taking part in a 30-fold increase of dust density. This is very similar to the concentrations that Rice et al. (2004) found in the spiral arms of self-gravitating disks.

In Figure 6 correlations between gas flow and particle density are shown for run D (without global pressure gradient). Here we have taken data at every full orbit, starting at five orbits when the turbulence has saturated, and calculated the average particle density in bins of various gas parameters. We also plot the spread in the particle density in each bin. The top two panels show the correlation with two components of the vorticity $\boldsymbol{\omega} = \nabla \times \boldsymbol{u}$. There is some correlation between the vertical vorticity component and the particle density, but the spread in each vorticity bin is larger than the average value. The correlation indicates that some trapping of particles is happening in anticyclonic regions and that regions of cyclonic flow are expelling particles (Barge & Sommeria 1995). Meter-sized particles should be optimally concentrated by vorticity, so the weak correlation between n and ω_z is surprising, considering that for centimeter-sized particles, JK05 find an

TABLE 2
RESULTS

Run (1)	$\Omega_0\tau_f$ (2)	β (3)	max (n) (4)	$\overline{v_x}$ (5)	$v_x^{(\mathrm{lam})}$ (6)	$\overline{\sigma}$ (7)	$\overline{\sigma_x}$ (8)	$\overline{\sigma_y}$ (9)	$\overline{\sigma_z}$ (10)
A	1.0	−0.04	81.3	−0.0123	−0.020	0.0222	0.0162	0.0105	0.0077
B	0.1	−0.04	32.6	−0.0034	−0.004	0.0139	0.0064	0.0101	0.0052
C	10.0	−0.04	77.5	−0.0042	−0.004	0.0170	0.0115	0.0094	0.0062
D	1.0	0.00	56.5	−0.0003	0.000	0.0225	0.0165	0.0106	0.0078
F	1.0	−0.04	50.3	−0.0132	−0.020	0.0204	0.0149	0.0093	0.0066
E	1.0	−0.04	50.3	−0.0132	−0.020	0.0194	0.0140	0.0086	0.0061

NOTES.—Col. (1): Name of run. Col. (2): Friction time. Col. (3): Global pressure gradient parameter. Col. (4): Maximum particle density in units of the average density. Col. (5): Radial velocity averaged over space and time. Col. (6): Predicted radial drift in a nonturbulent disk. Cols. (7)–(10): Velocity dispersion averaged over space and time. Averages are taken from five orbits and beyond. Grid cells with 0 or 1 particles have been excluded for the calculations of velocity dispersions.

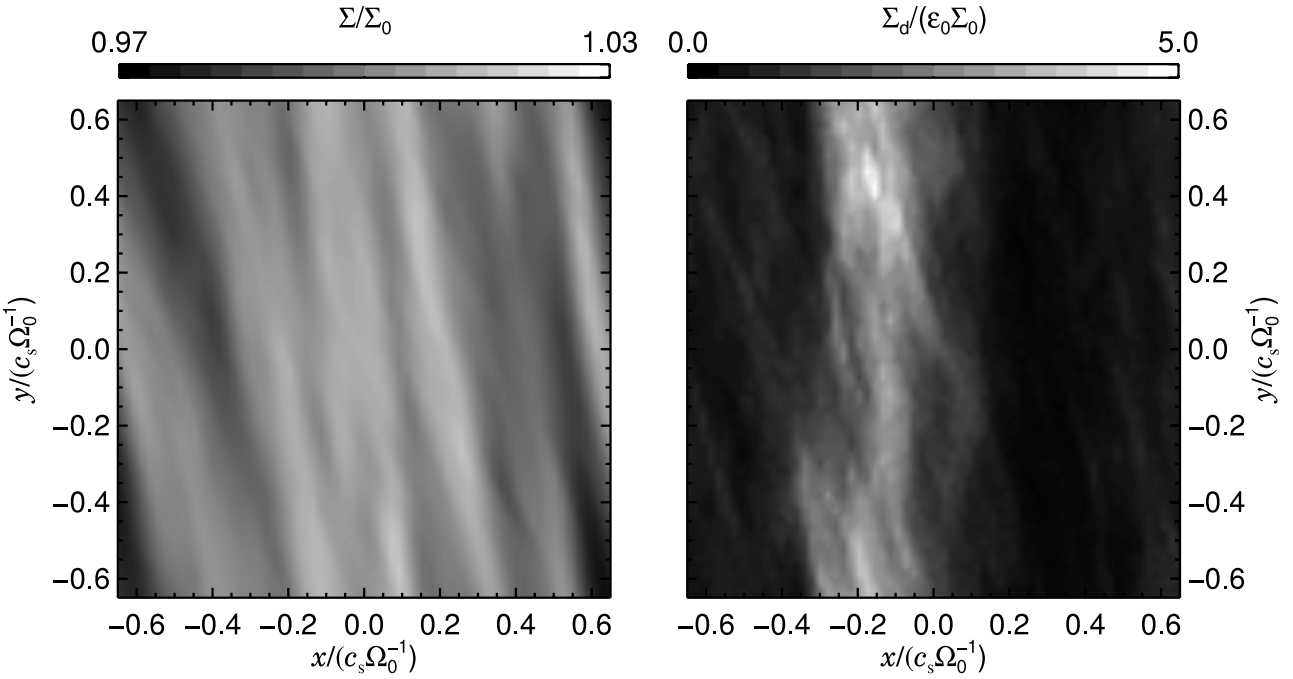

FIG. 3.—Gas column density Σ (*left*) and dust column density Σ_d (*right*). The gas column density only varies by a few percent over the box, but a slightly overdense region is still seen near the center of the box. The dust column density in the same region is up to 5 times the average dust column density.

almost linear relation between n and ω_z with very small spread. The explanation may be that the friction time is so high that particle concentrations stay together even after the gas feature that created them has decayed or moved to another location. The limited lifetime of the concentrating features weakens the measured correlation with the gas flow.

The bottom two panels of Figure 6 show the correlation with divergence of pressure gradient flux and with gas density. In a steady flow, particles accelerate toward an equilibrium velocity where the drag force is in balance with the other forces working on the particles. The equilibrium velocity is

$$\boldsymbol{v} = \tau_f \rho^{-1}(\nabla P - \boldsymbol{J}\times\boldsymbol{B}) \equiv \tau_f \boldsymbol{F}. \quad (14)$$

This is the mechanism for pressure gradient trapping. Places with a negative value of $\nabla\cdot\boldsymbol{F}$ should produce a high particle

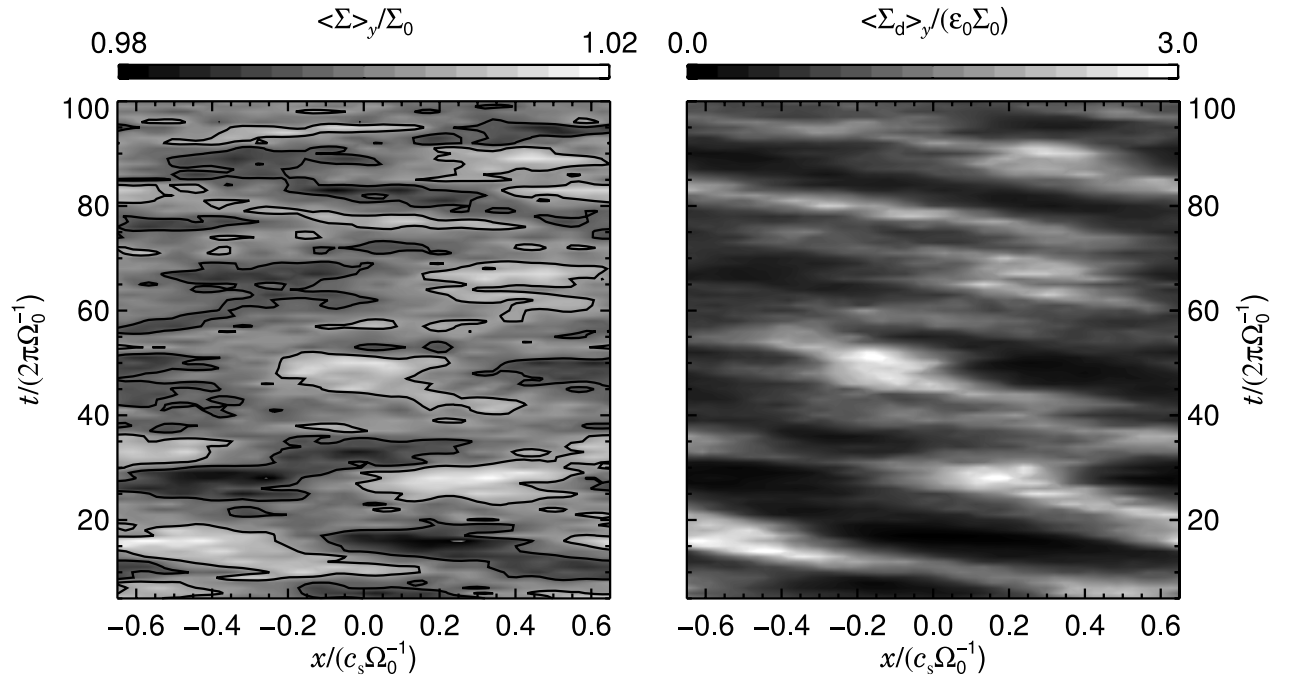

FIG. 4.—Azimuthally averaged gas and dust column densities as a function of radial position relative to the center of the box x and time t. Black contour lines are shown at gas density fluctuations of 0.5% from the average value. Large-scale density fluctuations are seen to have lifetimes on the order of a few orbits before moving to other radial positions. The dust column density peaks strongly at the locations of the maximal gas column density.

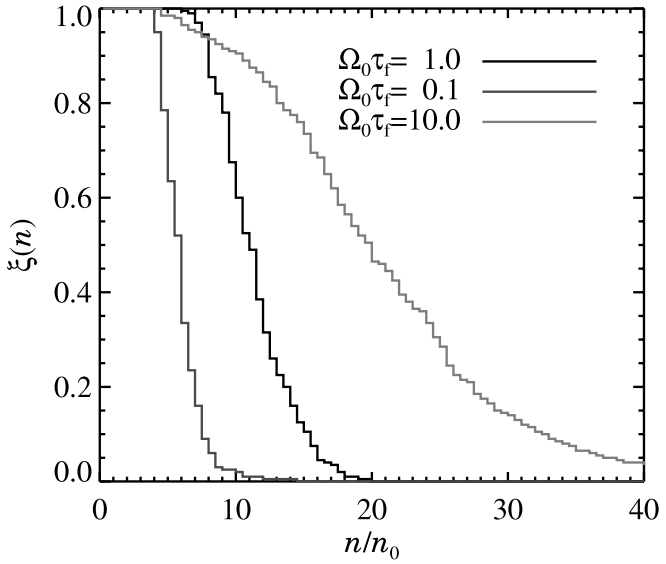

FIG. 5.—Distribution of maximum particle densities. The curves show the fraction $\xi(n)$ of particles that have been part of a given particle density during the 100 orbits. For $\Omega_0\tau_f = 0.1$, only concentrations up to 10 are common, whereas for $\Omega_0\tau_f = 1$, 70% of the particles have experienced at least a 10-fold increase in density. For massive boulders with $\Omega_0\tau_f = 10$, more than 10% were part of a 30-fold increase in density.

density (see JK05). The correlation between $\nabla \cdot \boldsymbol{F}$ and n is existent, but is very weak. The last panel, however, shows that there is a clear correlation between gas density and particle density, as is also evident from Figure 4. All in all, the correlations, even though some of them are quite weak, give the necessary information about the source of the dust concentrations. The concentrations are primarily due to pressure gradient trapping in the gas flow. There is also evidence of some vorticity trapping happening on top of that.

Increases in density of up to 2 orders of magnitude will make a difference in the coagulation process, because at places of larger concentration more collisions (both destructive and constructive) are possible. Also, there is a chance of increasing the density to such high values that a gravitational instability can occur in the densest places. We consider this last point in more detail in § 5. In § 4 we show that the turbulence not only causes concentrations, but also changes the radial drift velocity of the boulders.

4. DRIFT SPEED

The global pressure gradient on the gas forces solids to fall radially inward. If the gas motion in the disk were completely nonturbulent, then the equilibrium radial drift velocity arising from the head wind term present in equation (12) would be

$$v_x = \frac{\beta}{\Omega_0\tau_f + (\Omega_0\tau_f)^{-1}} c_s. \tag{15}$$

We derived this expression by solving for $\partial \boldsymbol{v}/\partial t = 0$ in equation (12). The highest drift speed occurs for particles with $\Omega_0\tau_f = 1$ with a laminar drift velocity of $v_x/c_s = \beta/2$. We have checked by putting particles of different friction times into a nonturbulent disk that the measured drift velocities are in complete agreement with equation (15).

The effect of a real turbulent disk on the average drift velocity is seen in Figure 7. Here the average radial velocity of all the particles is shown as a function of time for run A. For reference we overplot the laminar drift velocity ($v_x = -0.02c_s$) from equation (15) and the time-averaged drift velocity ($\overline{v_x} = -0.012c_s$). The mean drift velocity is noticeably affected by the turbulence, and its absolute value is reduced by 40% compared to the laminar value. The influence that turbulence can have on the mean drift velocity of the particles can be quantified with some simple analytical considerations. Considering the particles for a moment as a fluid with a number density scalar field n and a velocity

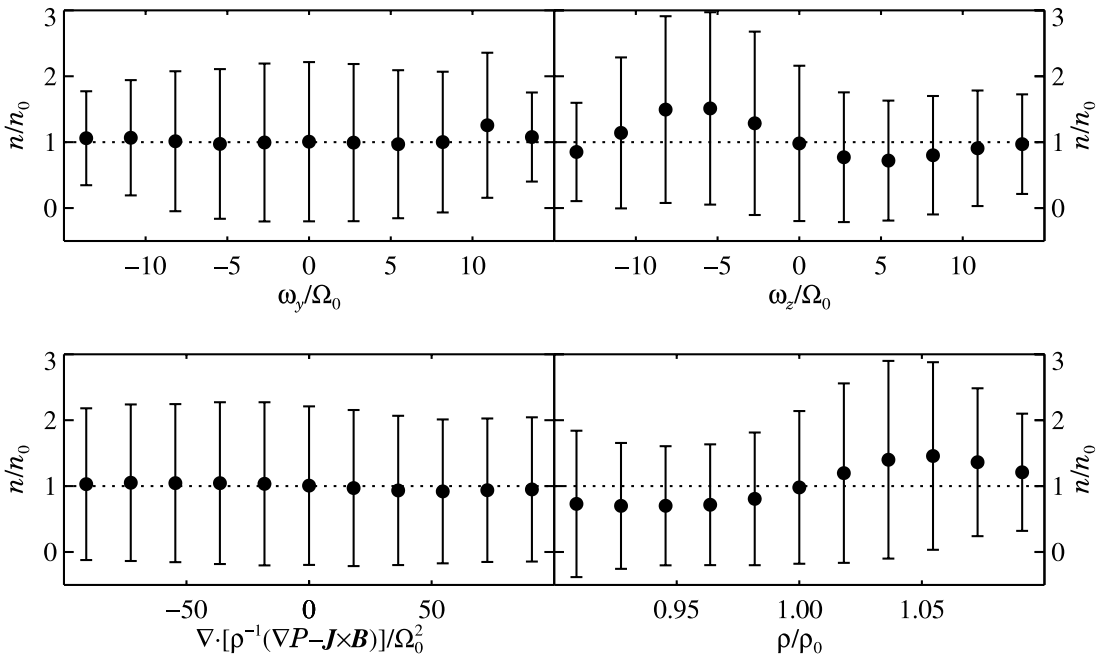

FIG. 6.—Correlations between particle number density and various gas parameters. The first row considers two components of the vorticity. There is some correlation between n and ω_z, indicating that particles are trapped in regions of anticyclonic flow. In the second row we consider the correlation between particle density and pressure gradient flux (explained in the text) and gas density, respectively. The first correlation is very weak, whereas there is evidently a correlation between gas density and particle density, although the fluctuation bars are significant.

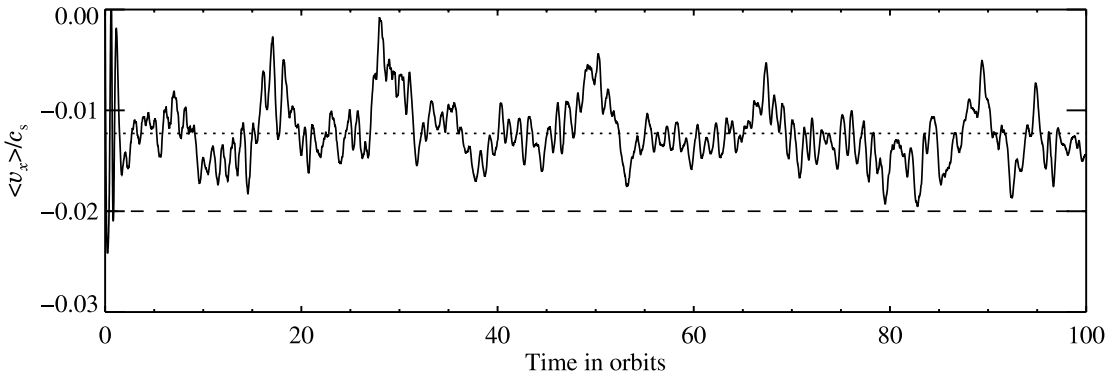

FIG. 7.—Average radial particle velocity as a function of time for meter-sized boulders. The nonturbulent drift velocity is $v_x^{(\mathrm{lam})} = -0.02c_s$ (*dashed line*), while the average drift velocity in the turbulent case is only around $\overline{v_x} = -0.012c_s$, a reduction of around 40% in speed.

vector field $\boldsymbol{w}$, the average radial velocity can be calculated with the expression

$$\langle w_x \rangle = \frac{\int_{x_0}^{x_1} n w_x \, dx}{\langle n \rangle L_x}. \tag{16}$$

Here we have weighted the drift velocity with the number density so that we are effectively measuring the average momentum. We consider now for simplicity particles that have been accelerated by the gas to their terminal velocity (eq. [15], including the fluctuation pressure gradient),

$$w_x = \epsilon c_s \left(\beta + H \frac{\partial \ln \rho}{\partial x} \right), \tag{17}$$

where ϵ is defined as $\epsilon = 1/[\Omega_0 \tau_f + (\Omega_0 \tau_f)^{-1}]$. Inserting now equation (17) into equation (16), the resulting drift velocity is found to consist of two terms,

$$\langle w_x \rangle = \epsilon \beta c_s + \frac{\epsilon c_s \int_{x_0}^{x_1} n (H \, \partial \ln \rho / \partial x) \, dx}{\langle n \rangle L_x}. \tag{18}$$

The first term on the right-hand side of equation (18) represents the contribution to the average drift velocity from the global pressure gradient (eq. [15]). The other term is an extra contribution due to any nonzero correlation between number density n and radial pressure gradient $\partial \ln \rho / \partial x$. This situation is sketched in Figure 8. Here we sketch the global density (*solid line*) and a sinusoidal density fluctuation $\ln \rho(x)$ (*dotted line*). Particles concentrate in regions where the gas density fluctuation is positive, because there the divergence of the particle velocity is negative. Due to the total pressure gradient, the newly produced particle clumps drift inward until the point where the outward drift toward the fluctuation density maximum balances the inward drift from the global pressure gradient. This is exactly around the location of the box in Figure 8. Here the correlation between n and $\partial \ln \rho / \partial x$ leads to a positive value of the integral in equation (18). A closer inspection of Figure 4 reveals that the dust overdensities are situated slightly downstream of the gas density fluctuation peaks, which is in good agreement with the prediction in Figure 8. If a significant fraction of the particles end up in such regions, the average drift speed is reduced.[2] For runs B and C, there is no significant reduction of the drift speed (see Table 2), but there the predicted drift speed is also 10 times lower than for meter-sized objects. Thus the measurement is not as reliable because the random velocity fluctuations of the particles dominate over the radial drift.

Due to the periodic boundary conditions in the y-direction, density structures quickly pass the y-boundaries, by shear advection, and thus possibly have some interference with themselves. To see the effect of the toroidal box size on the radial drift, we have run simulations with a box size of $1.32 \times 5.28 \times 1.32$ (run E) and $1.32 \times 10.56 \times 1.32$ (run F), keeping the resolution constant by adding the appropriate number of grid points in the y-direction. The time evolution of the mean radial drift velocity is shown in Figure 9. It is evidently very similar to Figure 7, so the toroidal size of the box does not influence the radial drift reduction noticeably. As seen in Table 2, the maximum particle density for runs E and F is quite high at 50 times the average density in the box, but not as high as in run A. However, simulations E and F only ran for 24 and 16 orbits, respectively, because of computational requirements due to the many grid points.

In simulations of the interaction between a planet and a magnetorotationally turbulent disk, Nelson & Papaloizou (2004)

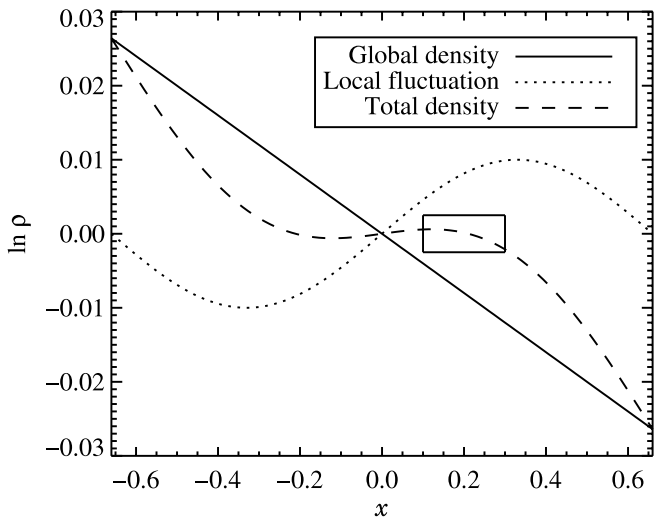

FIG. 8.—Sketch of how turbulent density fluctuations can cause the average drift velocity to change. The solid line shows the global density as a function of radial distance from the center of the box. On top of this we sketch a large-scale sinusoidal density fluctuation (*dotted line*) and the total density (*dashed line*). Dust particles are concentrated in the positive part of the fluctuation. At the same time, the concentration drifts toward the location of the box where the total drift speed is zero. If a significant fraction of the particles end up in such regions, then the average drift speed can decrease.

[2] A more graphic explanation of the speed reduction is to consider a car race over a distance of 100 km. Half of the distance is sand, where the cars can run 50 km hr^{-1}, and the other half asphalt, where the cars run 150 km hr^{-1}. The average speed of a single car reaching the finish line is less than 100 km hr^{-1}, simply because that car spent more time on sandy terrain than on asphalt.

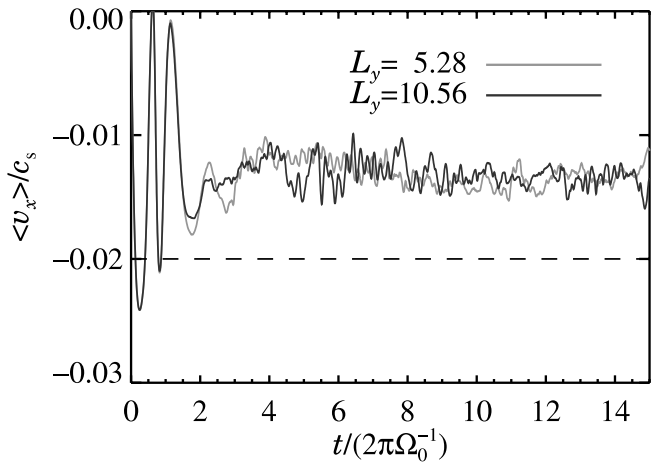

FIG. 9.—Drift velocity for simulations E and F with larger y-domains. The expected drift velocity in a laminar disk is indicated with a dashed line. The measured drift velocity is approximately the same as for the cube simulations, so the periodic y-boundary is not the reason for the reduced drift speed. Rather, it is a side effect of trapping the particles in radial density enhancements.

find that the average migration velocity of the planets is not changed by the presence of MRI turbulence (whereas the spread in drift velocity causes some planets to even drift outward). On the other hand, recent simulations by Nelson (2005) indicate that the mean migration of planets can indeed change because of turbulence. The fluctuations in migration speed are, however, much stronger than the average (so that hundreds of orbits are needed for a reliable estimate of the average). This is a very different kind of drift behavior than for the boulders in the current work, where the fluctuations in the drift speed are actually much *smaller* than the average. The presence of long-lived attracting regions in the gas may be the reason why boulders react to turbulence in a completely different way than planets do.

Diminishing the radial drift of meter-sized objects by roughly one-half may not be saving the boulders from their fate of decaying into the star. One would have to investigate this process by additionally looking at the growth behavior of the boulders that are sweeping up small grains on their way inward. This sweeping up is determined by the actual drift speed with respect to the local gas motion. Even if the mean drift speed is above the threshold for effective sticking, there will be phases of much lower radial drift, where growth can occur. The overdense regions would have a greatly increased rate of destructive encounters between larger bodies, and thus a large reservoir of small bodies, fed by the destructive collisions, could form. This would not only influence growth of larger bodies, but also possibly have observational consequences.

The present simulations are done in the gentle situation of turbulence in a local box. Global disk simulations have stronger turbulence and larger density fluctuations. One can predict that it would thus also lead to a larger decrease in radial drift speed. This would possibly give the meter-sized boulders enough time to grow to a size safe for radial drift. However, this has yet to be demonstrated in global simulations.[3]

[3] We have recently become aware of work done by Fromang & Nelson (2005), where the dynamics of boulders in magnetorotational turbulence is considered in global simulations of accretion disks. They found indeed that solids can be trapped inside persistent flow features for even 100 orbits, i.e., the entire simulation length.

5. GRAVITATIONAL INSTABILITY

We already showed that turbulence can strongly influence the growth of boulders by slowing them down and by concentrating them locally. These results can be incorporated into standard evolution codes for the solid material (e.g., Weidenschilling 1997; Dullemond & Dominik 2005), which try to grow planetesimals from dust grains via coagulation. On the other hand, the high local concentration can also lead to a different way of planetesimal formation, i.e., gelation. In the gelation case, a cloud of boulders is so dense that gravitational attraction becomes important. While we do not study self-gravity by an N-body approach in this work (as one should), we want to at least demonstrate by simple estimations under what conditions the concentration of boulders could clump into planetesimals.

The gravity constant G enters in self-gravity calculations, and thus the equations are no longer scale-free, but depend on the adopted disk model. We characterize a disk model by a column density Σ_0, an average dust-to-gas mass density ratio ϵ_0 (for boulders of the considered size range), and a scale height–to–radius ratio of ξ. Of course, ϵ_0 will be smaller than the global dust-to-gas ratio $\sim$0.02, because only a part of the mass will be present in boulders of the considered size range. We choose for simplicity the value $\epsilon_0 = 0.01$, assuming that 50% of the total dust mass is in bodies of the considered size, and we will later discuss how much this value is reasonable for a protoplanetary disk.

The apparently large number of particles in our numerical simulations is still orders of magnitude away from any real number of boulders in the volume of the protoplanetary disk that is considered. Thus it is necessary and valid to let one superparticle represent an entire swarm of many particles of similar location and velocity in the disk. Superparticle in this context means that one particle has the aerodynamic behavior of a single boulder, but represents a mass of trillions of such bodies as it mimics an entire swarm of protoplanetesimals. Similar assumptions are common in simulations of giant planet core formation from colliding planetesimals (Kokubo & Ida 2002; Thommes et al. 2003) as well as in cosmological N-body simulations (Sommer-Larsen et al. 2003). We let the simulation box represent the protoplanetary disk in the midplane. Each superparticle then contains the mass $m = \epsilon_1 \rho_1 V/N$, where V is the volume of the box, N is the number of superparticles, and ϵ_1 and ρ_1 are the dust-to-gas ratio and the gas density in the midplane of the disk. We use the isothermal disk expression $\rho_1 = \Sigma_0/(\sqrt{2\pi}H)$ to calculate the mass density in the midplane.

To calculate the dust-to-gas ratio in the midplane, ϵ_1, one needs to take into account the effect of vertical settling of solid material. Solids move in the direction of higher gas pressure. In the case of vertical stratification, this means that the boulders must sediment toward the midplane. An equilibrium is reached when the sedimentation is balanced by the turbulent diffusion, with diffusion coefficient D_t (Schräpler & Henning 2004), away from the midplane. This leads to a Gaussian profile of the dust-to-gas ratio (Dubrulle et al. 1995),

$$\epsilon = \epsilon_1 \exp\left[-z^2/(2H_\epsilon^2)\right], \tag{19}$$

with the dust-to-gas ratio scale height given by the expression $H_\epsilon^2 = D_t/(\tau_f \Omega_0^2)$. The dust-to-gas ratio at $z = 0$ is

$$\epsilon_1 = \epsilon_0 \sqrt{\left(\frac{H}{H_\epsilon}\right)^2 + 1}, \tag{20}$$

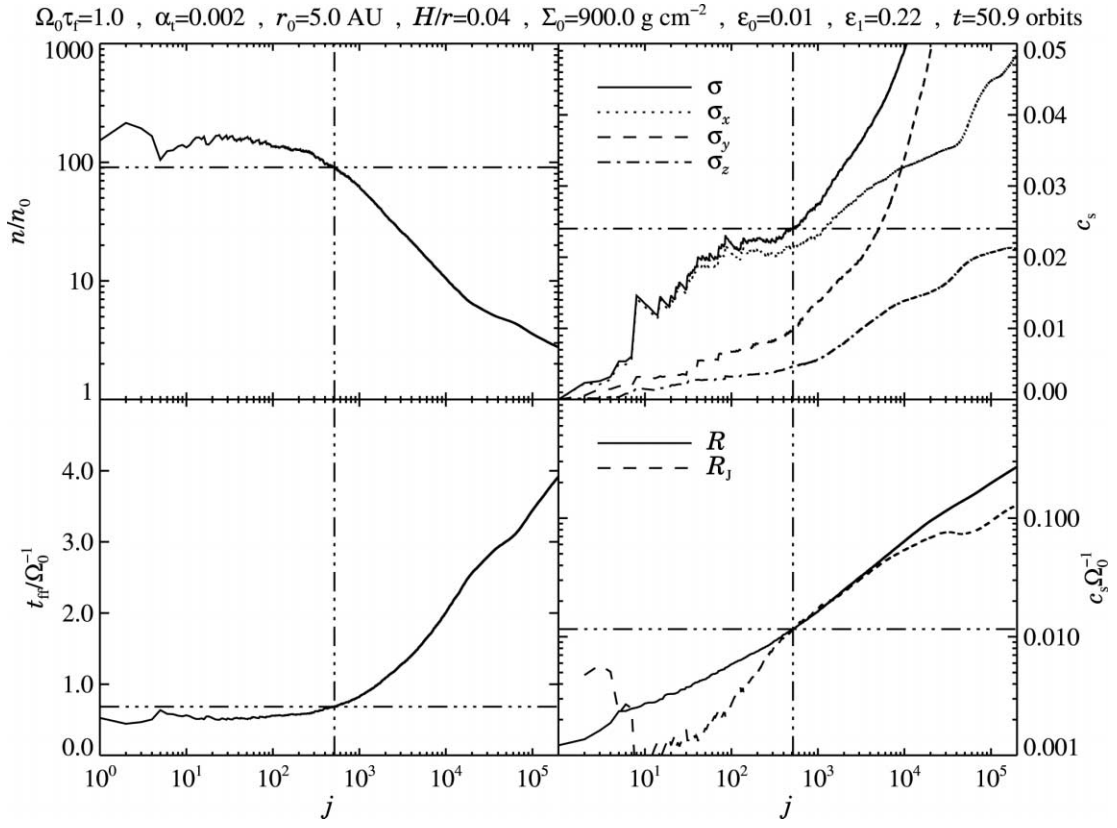

FIG. 10.—Particle number density n in units of average density n_0, velocity dispersion σ in units of sound speed c_s, free-fall time $t_{\rm ff}$ relative to the clump lifetime $t_{\rm cl}$, and clump radius R together with Jeans radius $R_{\rm J}$, all as a function of the number of included particles around the densest grid point in the box at a time of 50.9 orbits of run A. The vertical and horizontal triple-dot–dashed lines indicate the regions of gravitational instability for the choice of disk model parameters.

where $H = c_s\Omega_0^{-1}$ is the scale height of the gas. We now proceed by writing the turbulent diffusion coefficient as $D_t = \delta_t c_s^2 \Omega_0^{-1}$, where δ_t is the turbulent diffusion equivalent of α_t of Shakura & Sunyaev (1973). Then the midplane dust-to-gas ratio ϵ_1 can be written as

$$\frac{\epsilon_1}{\epsilon_0} = \sqrt{\frac{\Omega_0\tau_f}{\delta_t} + 1} \approx \sqrt{\frac{\Omega_0\tau_f}{\delta_t}}, \tag{21}$$

where the approximate expression is valid for $\Omega_0\tau_f \gg \delta_t$. For $\delta_t = \alpha_t = 0.002$ and $\Omega_0\tau_f = 1$, this gives $\epsilon_1 \approx 22.4\epsilon_0$, so starting from a dust-to-gas ratio of $\epsilon_0 = 0.01$, the midplane dust-to-gas ratio can be expected to rise to $\epsilon_1 = 0.22$ due to vertical settling. Such a low dust-to-gas ratio alone will not for any physically reasonable column density cause gravitational fragmentation (Goldreich & Ward 1973) or be subject to vertical stirring by the Kelvin-Helmholtz instability (the Richardson number [Ri] is around unity [see, e.g., Sekiya 1998], and stratification with Ri $>$ 0.25 should be stable). Even at such a high dust-to-gas ratio, we are still in the gas-dominated regime where the back-reaction from the dust on the gas can be neglected. The turbulent dust concentrations are assumed to occur in such a vertically settled dust layer. Now the most overdense regions will have a dust-to-gas ratio of unity and beyond. But we have measured that only about 3% of the grid cells have a dust-to-gas ratio of above unity at any given time, and thus it is still reasonable as a first approximation to ignore the back-reaction of the dust on the gas, although a more advanced study should include this effect as well.

To find out if a given overdense clump is gravitationally unstable, we compare the different timescales and length scales involved in fragmentation by self-gravity in a Jeans-type stability analysis. First we investigate whether the clump is gravitationally bound. We consider a clump of radius R, mass M, and velocity dispersion σ. The velocity dispersion must include the dispersion due to the background shear. For such a clump with a given mass to be gravitationally unstable, it must have a radius that is smaller than the Jeans radius given by

$$R_{\rm J} = \frac{2GM}{\sigma^2}\,. \tag{22}$$

If this first criterion is fulfilled, then it is also important that the collapse timescale of the structure is shorter than the lifetime of the overdense clump $t_{\rm cl}$. Only then we can be sure that the changing gas flow will not dissolve the concentration before it has had time to contract significantly. The fragmentational collapse happens on the free-fall timescale:

$$t_{\rm ff} = \sqrt{\frac{R^3}{GM}}\,. \tag{23}$$

The condition for gravitational instability is now that $R < R_{\rm J}$ and that at the same time $t_{\rm ff} < t_{\rm cl}$. We do not have to check separately that the collapse happens faster than a shear time $t_{\rm sh} = \Omega_0^{-1}$, since the effect of the background shear is already included in the velocity dispersion.

We now try to find out the smallest value of Σ_0 that gives rise to a gravitational instability. Then we can see whether or not this is a value that occurs in nature. For $\Omega_0\tau_f = 1$ (run A) the minimum value of the column density turns out to be around $\Sigma_0 =$ 900 g cm^{-2} (6 times the minimum mass solar nebula value at

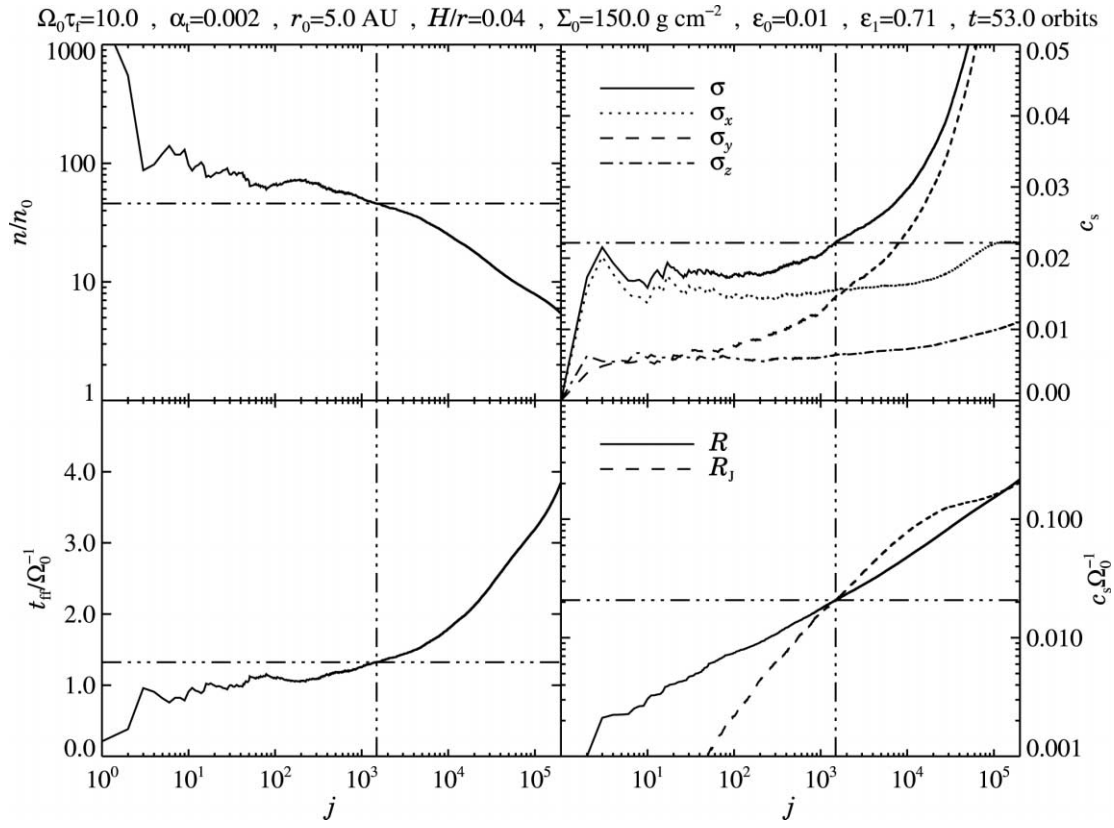

FIG. 11.—Same as Fig. 10, but for run C (decameter-sized bodies) at a time of 53 orbits. Here the minimum mass solar nebula column density is sufficient to have a gravitational instability. This is mainly because the velocity dispersion is smaller than for run A. In addition, the high-density region has a larger extent.

5 AU), whereas for $\Omega_0\tau_f = 10$ (run C), a gravitationally unstable cluster of protoplanetesimals is achieved already at the minimum mass solar nebula value $\Sigma_0 = 150$ g cm^{-2}.

First, run A is considered. Here we can calculate the mass in each superparticle. With $\Sigma_0 = 900$ g cm^{-2}, $\xi = 0.04$, $r = 5$ AU, and $\epsilon_1 = 0.22$, we get $\rho_1 = 1.2 \times 10^{-10}$ g cm^{-3} and $m = 8 \times 10^{20}$ g. Thus each superparticle represents about 3×10^{14} meter-sized protoplanetesimals. This is 5 orders of magnitude more mass than in a kilometer-sized planetesimal, but since we are interested in identifying gravitationally bound regions with the mass of thousands and thousands of planetesimals, this is not a problem. Actually, resolving the mass of even one single planetesimal with meter-sized objects would require on the order of a billion particles, which is way beyond current computational resources.

We examine the region around the densest grid point of run A at a time of $t = 50.9$ orbits in more detail. This time is chosen because a large concentration of particles occurs there; see Figure 1. We consider the j nearest particles to the densest point and calculate for j between 1 and 200,000 the particle number density n, the velocity dispersion σ and its directional components, the free-fall time $t_{\rm ff}$, and the radius of the clump together with the Jeans radius $R_{\rm J}$. The results are shown in Figure 10. It is reasonable to require at least $j = 100$ for a measurement to be statistically significant (for $j \geq 100$ the relative counting error falls below 10%; see, e.g., Casertano & Hut 1985). It is also reasonable to require that the size of the clump be larger than the size of a grid cell, since any structure in the concentration within a single cell is not well resolved. The same is true for the velocity dispersion. At $j = 100$ the dust number density is more than 130 times the average, but the radius of the $j = 100$ clump is only around 0.007, which is smaller than the grid cell radius of $\delta x/2 = 0.01$. At $j \simeq 500$ the clump has the size of a grid cell, and here the number density is more like 100 times the average. This must be multiplied by the enhancement by sedimentation, which is around 20, to give a dust-to-gas ratio increase by a factor of 2000 compared to the original value in the disk. The velocity dispersion is around $\sigma \sim 0.02c_s \ldots 0.03c_s$. That includes the velocity dispersion due to the background shear, but this is not a very important effect anyway because the size of the overdense clump is very small. At small scales the velocity dispersion is completely dominated by the radial component, according to Figure 10, whereas the shear only takes over at larger scales.

The free-fall time is a bit below the clump lifetime, which is typically 1 shear time (see inset in Fig. 1; note that the time unit is in orbits). For calculating the Jeans radius we have had to adopt a column density as high as $\Sigma_0 = 900$ g cm^{-2} in order to have the clump be gravitationally unstable. This is mainly due to the high-velocity dispersion. The radius of the clump is around 1 Jeans radius at $j = 1000$, so the clump is gravitationally bound at this scale and would be subject to further contraction by self-gravity. The gravitationally unstable region is around three grid cells in diameter, but even though this is well within the dissipative scales of the turbulence, the effect of the unresolved turbulence on the motion of the particles should be very little, as such small-scale turbulence has short lifetimes and low amplitudes compared to the large scales. Extrapolating the resolved large-scale turbulence to the grid scale with a Kolmogorov law gives lower turbulent velocities than the particle velocity dispersion that we already measure at the grid scale. Thus we conclude that the unresolved turbulence has little or no influence on the particle dynamics. The concentrations and velocity dispersions are exclusively driven by the large resolved scales of the gas motion.

The solid size of the forming object would be roughly 400 km if all the 1000 superparticles end up in just one large body. On the

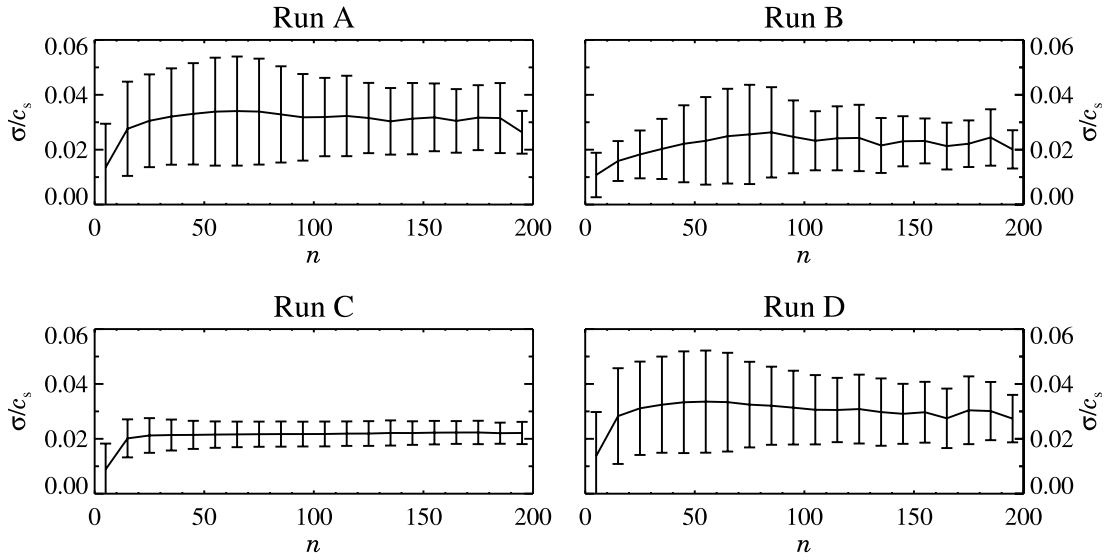

FIG. 12.—Average velocity dispersion and fluctuation interval as a function of the number of particles in a grid cell. The dispersion rises until there are around 50 particles in a grid cell and is then constant up to 200 particles, or around 30 times the average dust density. This corresponds to an isothermal equation of state for the boulders.

other hand, the outcome of such a collapse may also favor the further fragmentation of the clump. This all depends on how the velocity dispersion behaves with increasing density. In the *N*-body simulations of Tanga et al. (2004) gas drag works as an efficient way to dissipate the gravitational energy that is released in the contraction of protoplanetesimal clusters. Only such simulations that include self-gravity and gas drag could show the further evolution of the overdense boulder clumps that we see in the present work.

For decameter-sized bodies (run C), we plot in Figure 11 the same quantities as in Figure 10 around the densest point at a time of 53 orbits. This time we adopt the minimum mass solar nebula column density of $\Sigma_0 = 150$ g cm^{-2}, which gives a midplane density of $\rho_1 = 2 \times 10^{-11}$ g cm^{-3}. Because of the high friction time, the dust-to-gas ratio in the midplane (eq. [21]) is now 0.71. The Richardson number is correspondingly lower at around Ri = 0.4, so it is still stable to Kelvin-Helmholtz instability. The mass of the individual superparticles here is $m = 4 \times 10^{20}$ g. The density is slightly smaller than for meter-sized bodies, at statistically significant counts around 50 times the average, but the velocity dispersion is lower, and also the overdense region is much larger than it was for meter-sized boulders. Thus already a minimum mass solar nebula can produce a gravitational instability. The unstable region is as large as 10 grid cells in diameter and contains around 10^5 particles. The size of a solid object consisting of this number of superparticles is roughly 1400 km. Again there is also the possibility that millions of 10 km objects form instead.

The preceding calculations are of course only an estimation of the potential importance of self-gravity. In a real protoplanetary disk there will be a distribution of dust grain sizes present at any time. If, e.g., fragmentation is important, as discussed in § 1, then the greater part (80%) of the mass may still be present in bodies that are well below 1 m in radius (Dullemond & Dominik 2005). With only 20% of the mass in the size range between 1 and 10 m, the critical column density could be as much as a factor of 2 higher than stated above. However, this is still in the range of the masses derived for circumstellar disks. So the qualitative picture that the clumps are gravitationally unstable for physically reasonable gas column densities is robust.

To quantify the velocity dispersion in the entire box, we have calculated the average values over all the grid cells. The results are shown in the last four columns of Table 2. Grid cells with 0 or 1 particles have been excluded from the average because the velocity dispersion is per definition zero in these underresolved cells. The meter-sized bodies have the highest velocity dispersion, around $\sigma_1 \approx 0.02 c_s$, whereas decimeter bodies have $\sigma_{0.1} \approx 0.014 c_s$ and decameter bodies have a value of $\sigma_{10} \approx 0.017 c_s$. These values are similar to the turbulent velocities of the gas at the largest scales of the box (see Fig. 2 in JK05), which again shows that these large scales are the drivers of the particle dynamics. Interestingly, run D, which is similar to run A only without the radial pressure gradient, has the same velocity dispersion as run A, so the radial pressure gradient does not add extra velocity dispersion to the boulders. The toroidal component of the velocity dispersion is similar for all the runs because it is dominated by the shear over a grid cell. Run C has a radial velocity dispersion twice as large as run B. This can be explained because the large particles in run C react much slower to the local behavior of the gas, and thus particles of different velocities and histories are mixed in together.

The behavior of the velocity dispersion with increasing dust density is relevant for gravitational instability calculations. The average velocity dispersion, and the fluctuation width, as a function of the number of particles in a grid cell is shown in Figure 12. Again it is evident that the velocity dispersion for $\Omega_0 \tau_f$ of unity is largest. For all runs the velocity dispersion typically rises until there are around 50 particles in the cell. Then the dispersions stay constant all the way to 200 particles. Thus the equation of state of the particles is isothermal, at least up to 30 times the average dust density.

6. SUMMARY AND DISCUSSION

We have considered the effect of magnetorotational turbulence on the motion of dust particles with a freely evolving space coordinate. The particle treatment was necessary over the fluid treatment, because the mean free path of the macroscopic dust boulders is so long that they can no longer be treated as a fluid. The use of magnetorotational turbulence may not be completely justified in the midplane of the disk, where the ionization fraction

due to radiation and cosmic particles is low. But due to its Kolmogorov-like properties, where energy is injected at the unstable large scales and then cascades down to smaller and smaller scales, magnetorotational turbulence can be seen as a sort of "generic disk turbulence."

We find that the turbulence acts on the particles by concentrating meter-sized boulders locally by up to a factor of 100 and by reducing their radial drift by 40%. Both the concentrations and the reduced radial drift happen because the dust particles are temporarily trapped in radial density enhancements. One would not expect such structures to be long-lived in a general turbulent flow, but magnetorotational turbulence in accretion disks is subject to a strong shear that favors elongated toroidal structures. In the presented simulations the typical lifetime of the structures is on the order of a few orbits, corresponding to tens or even hundreds of years in the outer parts of a protoplanetary disk. When the density structures eventually dissolve, new structures appear at other locations. We find a strong correlation between a gas column density of a few percent above the average and a several times increase in the dust column density. We have also seen some evidence for increased dust density in regions of anticyclonicity, but the long friction time of the dust particles makes it difficult to identify the gas flow that caused a given concentration, because the concentration may drift away from the creation site.

The large concentrations naturally occur near the grid scale. In finite-resolution computer simulations the dissipative length scale must necessarily be moved from the extremely small dissipative scales of nature to the smallest scales of the simulation box. Thus the turbulence is not well resolved near the grid scale. On the other hand, the concentrations are driven by the largest scales of the turbulence, because these scales have the largest velocity amplitudes and the longest lived features (Völk et al. 1980). Already the other well-resolved but slightly smaller scales fluctuate too quickly and at speeds too low to influence the path of an object that is 1 m or larger in size. This argument is given support by the fact that we measure particle velocity dispersions in the grid cells that are comparable to the velocity amplitude of the gas at the largest scales of the simulation. Thus one should not expect higher resolution to change the concentrations or the velocity dispersions significantly.

Our estimation of the minimum gas column density that would make the densest protoplanetesimal clumps gravitationally unstable is necessarily based on many assumptions. We assumed that half of the dust mass in the disk was present in bodies of the considered size, whereas in real disks an even larger part of the dust mass may be bound in small fragments that result from catastrophic collisions. We also ignored the back-reaction from the dust on the gas. The background state has, both for meter and decameter bodies, a dust-to-gas ratio just below unity (where the back-reaction becomes important). The effect of dust drag on the magnetorotational instability has to our knowledge never been considered. One can speculate that the drag force will mimic a strong viscosity and thus disable the source of turbulence where the dust density is high. For the treatment of Kelvin-Helmholtz instability we based it simply on a criterion on the Richardson number Ri. There is some indication that this may be too simplistic and that in protoplanetary disks much higher Richardson numbers are also unstable (Gómez & Ostriker 2005), but one can also speculate that the full inclusion of dust particles in simulations of Kelvin-Helmholtz turbulence would show strong local concentrations like we see here for magnetorotational turbulence. Thus the exact values of 6 times the minimum solar nebula for meter-sized boulders and just the minimum mass solar nebula for decameter-sized boulders should only be considered as rough estimates. Still, the result that the clumps are gravitationally unstable for reasonable gas column densities is robust enough to warrant further investigations that include treatment of self-gravity between the boulders.

Thus we find that the gravoturbulent formation of planetesimals from the fragmentation of an overdense swarm of meter-sized rocks is possible. Turbulence is in this picture not an obstacle, but rather the ignition spark, as it is responsible for generating the local gravitationally bound overdensities in the vertically sedimented layer of boulders.

Computer simulations were performed at the Danish Center for Scientific Computing in Odense and at the RIO cluster at the Rechenzentrum Garching. Our research is partly supported by the European Community's Human Potential Programme, under contract HPRN-CT-2002-00308, PLANETS. We would like to thank the anonymous referee for a number of useful comments that helped to greatly improve the original manuscript.

REFERENCES

Balbus, S. A., & Hawley, J. F. 1991, ApJ, 376, 214
Barge, P., & Sommeria, J. 1995, A&A, 295, L1
Beckwith, S. V. W., Henning, Th., & Nakagawa, Y. 2000, in Protostars and Planets IV, ed. V. Mannings, A. P. Boss, & S. S. Russell (Tucson: Univ. Arizona Press), 533
Blum, J., & Wurm, G. 2000, Icarus, 143, 138
Brandenburg, A. 2003, in Advances in Nonlinear Dynamos, ed. A. Ferriz-Mas & M. Núñez (London: Taylor & Francis), 269
Casertano, S., & Hut, P. 1985, ApJ, 298, 80
Chavanis, P. H. 2000, A&A, 356, 1089
Chokshi, A., Tielens, A. G. G. M., & Hollenbach, D. 1993, ApJ, 407, 806
Cuzzi, J. N., Dobrovolskis, A. R., & Champney, J. M. 1993, Icarus, 106, 102
de la Fuente Marcos, C., & Barge, P. 2001, MNRAS, 323, 601
Dominik, C., & Tielens, A. G. G. M. 1997, ApJ, 480, 647
Dubrulle, B., Morfill, G., & Sterzik, M. 1995, Icarus, 114, 237
Dullemond, C. P., & Dominik, C. 2005, A&A, 434, 971
Fromang, S., & Nelson, R. P. 2005, MNRAS, 364, L81
Fromang, S., Terquem, C., & Balbus, S. A. 2002, MNRAS, 329, 18
Gammie, C. F. 1996, ApJ, 457, 355
Goldreich, P., & Tremaine, S. 1978, ApJ, 222, 850
Goldreich, P., & Ward, W. R. 1973, ApJ, 183, 1051
Gómez, G. C., & Ostriker, E. C. 2005, ApJ, 630, 1093
Haghighipour, N., & Boss, A. P. 2003, ApJ, 583, 996
Henning, Th., Dullemond, C. P., Dominik, C., & Wolf, S. 2006, in Planet Formation: Observations, Experiments, and Theory, ed. H. Klahr & W. Brandner (Cambridge: Cambridge Univ. Press), in press
Hodgson, L. S., & Brandenburg, A. 1998, A&A, 330, 1169
Johansen, A., Andersen, A. C., & Brandenburg, A. 2004, A&A, 417, 361
Johansen, A., & Klahr, H. 2005, ApJ, 634, 1353 (JK05)
Klahr, H. 2004, ApJ, 606, 1070
Klahr, H., & Bodenheimer, P. 2003, ApJ, 582, 869
Klahr, H., & Lin, D. N. C. 2001, ApJ, 554, 1095
———. 2005, ApJ, 632, 1113
Klessen, R. S., Heitsch, F., & Mac Low, M. 2000, ApJ, 535, 887
Kokubo, E., & Ida, S. 2002, ApJ, 581, 666
Lissauer, J. J. 1993, ARA&A, 31, 129
Nakagawa, Y., Sekiya, M., & Hayashi, C. 1986, Icarus, 67, 375
Nelson, R. P. 2005, A&A, 443, 1067
Nelson, R. P., & Papaloizou, J. C. B. 2004, MNRAS, 350, 849
Paardekooper, S.-J., & Mellema, G. 2004, A&A, 425, L9
Padoan, P., & Nordlund, Å. 2004, ApJ, 617, 559
Rice, W. K. M., Lodato, G., Pringle, J. E., Armitage, P. J., & Bonnell, I. A. 2004, MNRAS, 355, 543
Safronov, V. S. 1969, Evoliutsiia doplanetnogo oblaka. (English transl., Evolution of the Protoplanetary Cloud and Formation of Earth and the Planets [NASA Tech. Transl. F-677; Jerusalem: Israel Sci. Transl. (1972)])
Schräpler, R., & Henning, T. 2004, ApJ, 614, 960

Sekiya, M. 1998, Icarus, 133, 298
Semenov, D., Wiebe, D., & Henning, T. 2004, A&A, 417, 93
Shakura, N. I., & Sunyaev, R. A. 1973, A&A, 24, 337
Sommer-Larsen, J., Götz, M., & Portinari, L. 2003, ApJ, 596, 47
Suttner, G., & Yorke, H. W. 2001, ApJ, 551, 461
Tanga, P., Weidenschilling, S. J., Michel, P., & Richardson, D. C. 2004, A&A, 427, 1105
Thommes, E. W., Duncan, M. J., & Levison, H. F. 2003, Icarus, 161, 431
Völk, H. J., Morfill, G. E., Roeser, S., & Jones, F. C. 1980, A&A, 85, 316
Weidenschilling, S. J. 1977, MNRAS, 180, 57
———. 1980, Icarus, 44, 172
———. 1984, Icarus, 60, 553
———. 1997, Icarus, 127, 290
Weidenschilling, S. J., & Cuzzi, J. N. 1993, in Protostars and Planets III, ed. E. H. Levy & J. I. Lunine (Tucson: Univ. Arizona Press), 1031
Wetherill, G. W. 1990, Icarus, 88, 336
Wurm, G., Blum, J., & Colwell, J. E. 2001, Icarus, 151, 318
Youdin, A. N., & Shu, F. H. 2002, ApJ, 580, 494